

Empirical Validation of a Class of Ray-Based Fading Models

Juan E. Galeote-Cazorla, Alejandro Ramírez-Arroyo, F. Javier Lopez-Martinez and Juan F. Valenzuela-Valdés

Abstract—As new wireless standards are developed, the use of higher operation frequencies comes in hand with new use cases and propagation effects that differ from the well-established state of the art. Numerous stochastic fading models have recently emerged under the umbrella of *generalized fading* conditions, to provide a fine-grain characterization of propagation channels in the mmWave and sub-THz bands. For the first time in literature, this work carries out an experimental validation of a class of such ray-based models, in a wide range of propagation conditions (anechoic, reverberation and indoor) at mmWave bands. We show that the independent fluctuating two-ray (IFTR) model has good capabilities to recreate rather dissimilar environments with high accuracy. We also put forth that the key limitations of the IFTR model arise in the presence of reduced diffuse propagation, and also due to a limited phase variability for the dominant specular components.

Index Terms—channel characterization, stochastic fading channels, IFTR, GTR-V, anechoic chamber, reverberation chamber, indoor environments

I. INTRODUCTION

The advent and widespread deployment of the fifth generation (5G) of wireless technology has been key to improve the achievable data rates well-beyond tenths of Gbps, and also to reduce latency in one order of magnitude with respect to previous standards – now approaching to 1 ms [1]. One of the key enablers for such achievements is the use of higher frequency bands in the millimeter wave (mmWave) range. This trend is likely to continue as 5G evolves, and sixth generation (6G) is often envisioned to provide coverage in the sub-THz range for some use cases [2].

To properly modeling and describing propagation channels, different approaches can be taken to capture the true (and often intractable) nature of electromagnetic effects as signals traverse the wireless environment. Classically, channel

modeling strategies have been categorized as empirical vs. analytical, and also as deterministic vs. stochastic [3]. Today, state-of-the-art channel models combine the key features from these approaches to improve accuracy. For instance, COST [4] and 3GPP-like [5] models combine empirical measurements (e.g. for path-loss exponents) with geometric modeling of the propagation environment, also incorporating some stochastic features to provide randomness inherent to wireless fading effects. These models often have hundreds of parameters that allow to recreate wireless propagation with high versatility, at the expense of a higher complexity and computational burden. Recently, ray-tracing approaches have been considered as an alternative to provide a realistic channel characterization in terms of a number of multipath components (MPCs) [6], at the price of an overwhelming mathematical complexity.

To circumvent the intricacy of these approaches, analytical stochastic channel models are of widespread use due to their comparatively reduced complexity, much fewer parameters, and mathematical tractability [7]. Rayleigh and Rician models are immensely popular in the wireless community, as the de facto standards to model small-scale fading in non line-of-sight (nLoS) and line-of-sight (LoS) cases, respectively. As new use cases promote the ubiquity of wireless devices, many new environments in sensor networks and industrial settings require the development of more advanced models¹, often referred to as *generalized*. For instance, the two-wave with diffuse power (TWDP) model [8] proposed by Durgin, Rappaport and de Wolf describes a multipath environment with two dominant constant-amplitude specular rays, plus an aggregate diffuse component. With only one parameter addition compared to the Rician case, the TWDP model has an increased capability to recreate not-so-common propagation conditions; these include bimodality and hyper-Rayleigh behavior [9]. Subsequently, different generalizations and alternatives have been proposed in the literature: for instance, the fluctuating two-ray (FTR) model [10] allows that the two rays of the TWDP model fluctuate *jointly* or *independently* [11]. This philosophy is inherited from Abdi's Rician-shadowed model [12], which also generalizes the Rician one. The κ - μ and the η - μ models proposed by Yacoub add additional flexibility to the Rician and Rayleigh models through the notion of multipath wave clusters. These were also later generalized by Paris' κ - μ shadowed fading model [13].

Recently, it was shown that it is possible to bridge the gap

¹While any distribution borrowed from statistics may be used to approximate the behavior of wireless channels, only a certain class of distributions that comply with electromagnetic propagation laws will capture the true nature of communications channels.

This work has been supported by grant TED2021-129938B-I00 funded by MCIN/AEI/10.13039/501100011033 and by the European Union NextGenerationEU/PRTR. It has also been supported by grants PID2020-112545RB-C54, PDC2022-133900-I00, PDC2023-145862-I00 and TED2021-131699B-I00, funded by MCIN/AEI/10.13039/501100011033 and by the European Union NextGenerationEU/PRTR; in part by Junta de Andalucía through grant EMERGIA20-00297; and in part by the predoctoral grant FPU22/03392. (Corresponding author: Juan E. Galeote-Cazorla).

Juan E. Galeote-Cazorla, F. Javier Lopez-Martinez and Juan F. Valenzuela-Valdés are with the Dept. Signal Theory, Networking and Communications, Research Centre for Information and Communication Technologies (CITIC-UGR), University of Granada, 18071, Granada, Spain. F. Javier Lopez-Martinez is also with the Communications and Signal Processing Lab, Telecommunication Research Institute (TELMA), Universidad de Málaga, Málaga, 29010, Spain (e-mails: juane@ugr.es; fjlm@ugr.es; juanvalenzuela@ugr.es)

Alejandro Ramírez-Arroyo is with the Department of Electronic Systems, Aalborg University (AAU), 9220 Aalborg, Denmark (e-mail: araar@es.aau.dk).

between the models used for industry (e.g., 3GPP TR 38.901) and academia (e.g., ray based), by developing a multiple-inputs multiple-outputs (MIMO) channel model that calibrates the few parameters of the latter using the full 3GPP TR 38.901 channel model as a reference [14]. Clearly, the key to use any of the aforementioned statistical models for 5G performance evaluation in practical conditions is their empirical validation over a great variety of scenarios. One way to accomplish this is through measurement campaigns on a specific scenario; for instance, mobile radio channels over the sea at 5.9 GHz or vehicular channels during overtakes at 60 GHz exhibit TWDP behaviors [15, 16]. However, such campaigns are rather costly in terms of time and resources, and cannot be replicated in a controlled way. Another alternative is the use of laboratory chambers combining anechoic and reverberation features. These allow to recreate Rician-fading [17] or two-ray [18] environments, which can be exploited to emulate MIMO channels with such particular behavior [19].

In this paper, we aim to empirically validate a class of ray-based stochastic fading models in a wide variety of scenarios. Specifically, we used our mixed anechoic/reverberation chamber facilities, together with indoor acquisition, to find a concordance between measurements and different propagation models in the frequency band from 24.25 GHz to 27.5 GHz (i.e., 3GPP n258 band), which belongs to the mmWave general classification [5]. For this purpose, we consider the independent fluctuating two-ray (IFTR) fading model recently proposed in [11], showing a remarkable goodness of fit in most scenarios. Interestingly, we identify that the widespread assumption of uniform phases for the two dominant specular components [8] does not hold in some scenarios with reduced multipath. We show that in those scenarios where this behavior is identified, a more general modeling for the phases [21] improves the fitting performance.

The remainder of the article is organized as follows. Section II summarizes the IFTR propagation model with the relevant physical and mathematical basis. Section III explains how the measurements were acquired and how they are used for recreating new scenarios. Section IV shows and discuss the obtained results from fitting the scenarios with the propagation models. Finally, Section V summarizes the key conclusions and the future lines derived from this work.

II. PHYSICAL CHANNEL MODEL

Let us consider a general formulation for the received radio signal over a wireless channel [22], given as a superposition of a number of waves

$$V_r = \sum_{n=1}^M A_n \exp(j\varphi_n), \quad (1)$$

where A_n and φ_n denote their corresponding amplitudes and phases. Now, it is possible to rewrite (1) in the following way:

$$V_r = \sum_{n=1}^N A_n \exp(j\varphi_n) + \underbrace{\sum_{m=1}^P A_m \exp(j\varphi_m)}_Z, \quad (2)$$

with $M = N + P$, so that N now represents a group of dominant specular waves, while P indicates a group of numerous and relatively weak diffusely propagating waves. For sufficiently large P , the central limit theorem (CLT) holds for the second term in (2), implying that $Z \triangleq \sum_{m=1}^P A_m \exp(j\varphi_m)$ can be approximated as a complex Gaussian random variable (RV) with zero-mean and variance $2\sigma^2$. For $N = 2$, constant-amplitude A_n and uniformly distributed phases φ_n , the TWDP model emerges [8]. In the sequel, and taking the TWDP model as a baseline reference, we consider the general case on which $A_n = V_n \sqrt{\xi_n}$ so that V_n denotes the amplitude of each of these dominant specular components, whereas ξ_n are unit-mean independent Gamma RVs characterizing amplitude fluctuations. This model, referred to as IFTR model, was recently formulated in [11], and is fully characterized by the following set of parameters:

$$K = \frac{V_1^2 + V_2^2}{2\sigma^2} \in [0, \infty), \quad (3)$$

$$\Delta = \frac{2V_1 V_2}{V_1^2 + V_2^2} \in [0, 1], \quad (4)$$

$$m_n \{n = 1, 2\} \in (0, \infty), \quad (5)$$

$$\Omega \triangleq E\{|V_r|^2\} \in [0, \infty), \quad (6)$$

where $1/m_n$ denotes the fading severity (i.e., the amount of fluctuation) for each of the specular components, K is the Rician factor defined as the ratio between the average powers of the dominant specular waves and the diffuse components, and Δ captures the amplitude dissimilarity between the two dominant specular waves. Finally, the scale parameter $\Omega = V_1^2 + V_2^2 + 2\sigma^2$ represents the average received power.

A closed-form expression for the probability density function (PDF) $f_r(r)$ of the received radio signal magnitude $r = |V_r|$ can be found in (7). It is expressed in terms of the parameters defined in eqs. (3)-(6) and the confluent hypergeometric function $\Phi_2^{(n)}(\cdot)$ [23]. This expression is only valid when m_1 and m_2 take integer values. Nevertheless, every positive real value can be evaluated by computing the numerical inverse Laplace transform over the moment generating function (MGF) [11]. Moreover, a new analytical PDF based on mixture of Gamma distributions has been recently proposed in [24].

The main advantage of these ray-based statistical models is their physical interpretability. Models such as the mixture of distributions (e.g. Gaussian or Gamma mixture models [25], [26]) can fit experimental data with arbitrary precision. However, they lack any physical interpretation as the number of involved distributions increases. In contrast, models such as the IFTR only need a reduced set of parameters with a clear physical meaning as previously discussed. They allow us to characterize channels in terms of their physical behavior.

III. MEASUREMENTS ANALYSIS

The studied measurement dataset consists in the channel frequency response obtained for three different scenarios, namely: (semi)-anechoic and (semi)-reverberation chambers, and indoor. A more extensive description of the channel environments can be consulted in [27]. They were

$$\begin{aligned}
f_r(r) = & \frac{2r(1+K)}{\Omega} m_1^{m_1} m_2^{m_2} \left(m_1 + \frac{K}{2} (1 + \sqrt{1 - \Delta^2}) \right)^{m_2 - m_1} \sum_{n=0}^{m_1 - 1} \frac{1}{n!} \binom{m_1 - 1}{n} \frac{\Gamma(m_2 + n)}{\Gamma(m_2)} \left(\frac{K\Delta}{2} \right)^{2n} \\
& \times \left[m_1 \frac{K}{2} (1 - \sqrt{1 - \Delta^2}) + m_2 \frac{K}{2} (1 + \sqrt{1 - \Delta^2}) + m_1 m_2 \right]^{-m_2 - n} \\
& \times \Phi_2^{(3)} \left(n + 1 - m_1, m_1 - m_2, m_2 + n; 1; -\frac{1+K}{\Omega} r^2, -\frac{m_1(1+K)}{(m_1 + K/2(1 + \sqrt{1 - \Delta^2}))\Omega} r^2, \right. \\
& \left. -\frac{m_1 m_2(1+K)}{(m_1 K/2(1 - \sqrt{1 - \Delta^2}) + m_2 K/2(1 + \sqrt{1 - \Delta^2}) + m_1 m_2)\Omega} r^2 \right). \quad (7)
\end{aligned}$$

taken at the Smart and Wireless Applications and Technologies (SWAT) research group facilities, located at the University of Granada (Spain). Acquisition was performed with a vectorial network analyzer (VNA Rohde & Schwarz ZVA67) as the channel sounder, which is capable of measuring the S-parameters up to 67 GHz. The analyzed frequency band sweeps from 24.25 GHz to 27.5 GHz with a 5 MHz step, that is 651 points. It corresponds with the 3GPP n258 band, included in the mmWave classification. Standardized gain horns were used as transmitter (Tx) and receiver (Rx) antennas, specifically the Flann K-band antenna model #21240-20 fed with a WR-34 waveguide-to-coaxial transition. Finally, the transmission power was set to 10 dBm.

As previously mentioned, two of the scenarios were measured in a half anechoic-half reverberation chamber whose dimensions are $5 \times 3.5 \times 3.5$ meters (see Fig. 1). The semi-anechoic side is completely covered with absorbers to suppress any possible reflection in order to receive the ray from the LoS path exclusively. In contrast, the semi-reverberation side is composed entirely of metallic walls favoring the appearance of multiple reflections. The emerged behavior corresponds with a multipath channel. In contrast, the indoor scenario is slightly different. It corresponds with the experimental laboratory of the research group, where the chamber is located. In this case, the scenario represents by itself a real environment for communications, whereas the measurements in chambers can be used for the emulation of new channels.

The measuring setup for the semi-anechoic chamber consists of both Tx and Rx in LoS configuration with a distance between each other of 160 cm. The Rx antenna describes an 11×11 virtual uniform rectangular array (URA) over the XZ plane with a constant separation of 4 cm between the elements. On the other hand, the Tx antenna sweeps three azimuth angles ϕ : 0° and $\pm 30^\circ$, where the angle 0° corresponds with the perpendicular line pointing to the XZ plane. In addition, three roll angles β are swept: 0° and $\pm 30^\circ$, where now the angle 0° represents the situation with no-depolarization losses. This implies 3×3 different configurations for the Tx antenna and a total number of point-to-point measured channels of $11 \times 11 \times 3 \times 3 = 1089$. These propagation measurements are characterized by a single ray and a reduced diffuse power due to the absorbers.

In the semi-reverberation chamber, the setup changes to a nLoS situation where the Tx antenna is pointing to the

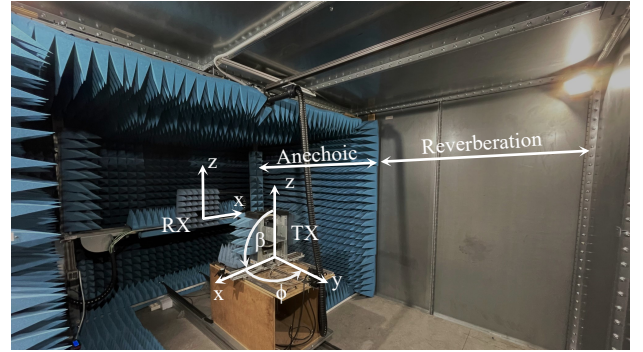


Fig. 1. Panoramic picture of the half anechoic-half reverberation chamber. The receiver antenna can move over the hole XZ plane. However, the transmitter only modifies the ϕ and β angles, named azimuth and roll respectively, for changing orientation and polarization.

reverberation side of the chamber (see Fig. 1). Now, the distance between the antennas is 600 cm, measured as the sum of the distances of each antenna to the metallic wall parallel to the XZ plane. The Tx and Rx antenna configurations are analogous to those described for the anechoic chamber, obtaining additional 1089 channel measurements. For this case, the azimuth angle $\phi = 0^\circ$ represents the situation where the Tx antenna points to the metallic wall parallel to the XZ plane. In this scenario, multipath channels are generated where up to seven reflections are identified in our experiments depending on the Tx-Rx configuration. Since it is a semi-reverberation chamber, the measurements involve several individual rays instead of a continuous reception as one would expect in a full reverberation chamber. This is a consequence of the absorption at the anechoic side. Each ray has a particular power that can be significantly higher than the noise floor or comparable to it, classifying them as specular or diffuse components respectively.

Finally, in the indoor setup the Tx antenna is located inside the chamber pointing outside to the Rx antenna in LoS, which is positioned inside the laboratory room (an illustrative figure can be found in [27]). The Rx describes the same virtual URA as for the chamber scenarios. However, the Tx changes the azimuth angle ϕ , now sweeping -30° , -15° , and 0° for exclusively pointing outside the chamber in a LoS situation. The swept β angles have no changes: $\pm 30^\circ$ and 0° . Thus, the total number of measured channels for the indoor scenario is

also 1089. As a complex environment, several specular and diffuse components are received with the LoS ray.

A TOSM (Through - Open - Short - Match) calibration process has been performed, setting the calibration planes at the end of the coaxial lines that connect the VNA with the horn antennas. Thus, all the acquired measurements include the antenna gain patterns as components of the propagation channel. Then, we can admit that the channel response $H(f)$ is equivalent to the measured transmission parameter $S_{21}(f)$. On the other hand, the received signal $Y(f)$ from a linear and time-invariant system can be computed as $Y(f) = H(f)X(f)$, where $X(f)$ is the transmitted signal. If we assume that $X(f) = 1$ V, we can admit that all the VNA measurements are expressed in terms of volts. Additionally, each of the 651 frequency points can be considered as an individual realization of the channels because of the static conditions of the environments during the measurement process.

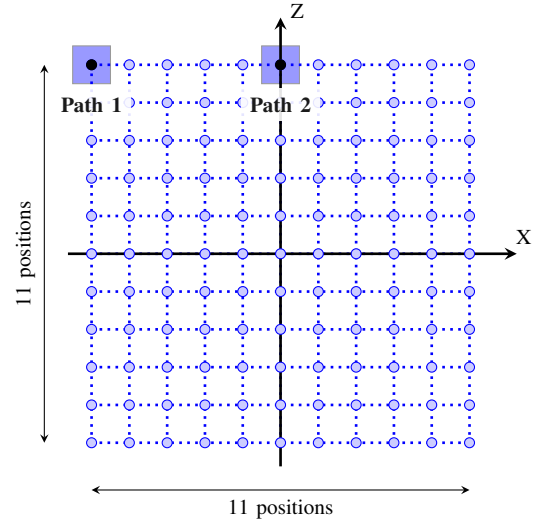
The described setups have resulted in 1089 channel measurements per scenario² (anechoic, reverberation and indoor). By construction, the chamber scenarios may not resemble propagation channels with more than one specular dominant component for communications. Nevertheless, more complex scenarios can emerge from the combination of the original measurements. Note that similar approaches are carried out in the literature to generate synthetic array geometries from individual measurements [28]. A simple application of this methodology is followed for this work. If we denote $H_1(f)$ and $H_2(f)$ as two different channel measurements from the same original scenario, we can compute a more complex channel $\hat{H}(f)$ by performing an equally-weighted linear combination as follows:

$$\hat{H}(f) = H_1(f) + H_2(f). \quad (8)$$

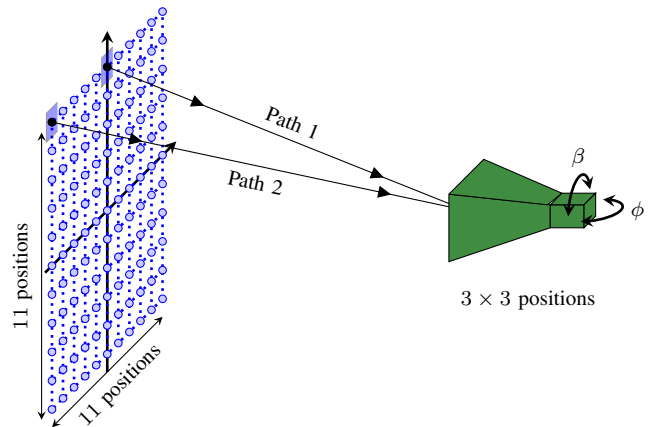
In the anechoic case a low diffuse power and the presence of only one relevant ray are expected. When two measurements are combined by applying (8), the resulting channel may reproduce scenarios where the diffuse power is reduced and only one or two rays are received in a LoS situation, emulating the two-ray scenario conditions intrinsic to the IFTR model. On the other hand, the reverberation case has a strong diffuse power with the presence of multiple rays. The combination of channels may resemble an industrial environment where nLoS situations are common and reflections over metallic surfaces are the main propagation mechanisms. Additionally, linear combinations may also be performed for the indoor measurements. In this case, the advantage relies on the increase of channel diversity since it is equivalent to introducing new reflections or additional diffuse power sources. The fitting of the IFTR model with these measurements allow us to validate it in realistic scenarios.

For giving physical coherence to the linear combinations, the channels $H_1(f)$ and $H_2(f)$ have to share the same transmitter orientation or receiver position. That is, if we combine two channels with different Rx array positions, the

²We are focusing on point-to-point measurements. However, this setup might be used for studying MIMO systems by synthesizing arbitrary planar array geometries [28]. Moreover, performance comparisons between distributed and centralized MIMO might be carried out.



(a) Selection of two different positions in the receiver array.



(b) Transmitter orientation of 0° in azimuth and roll angles.

Fig. 2. Channel combination example (configuration A) of two receiver positions linked to the same transmitter orientation.

corresponding Tx orientations must be the same. Similarly, if we take two channels with different Tx orientations, they must be linked to the same Rx array position. Fig. 2 shows one combined or merged channel example under this criterion, named configuration A in the following. Two positions in the Rx array are selected as in Fig. 2(a). Then, one Tx orientation is fixed for both positions as in Fig. 2(b).

The number of possible pairs of linear combinations becomes unmanageable since it is in the order of hundreds of thousands³. This fact implies that only a reduced sample of all the possible combinations shall be selected [29], searching for a compromise between the number of configurations and the total execution time of the IFTR model validation process. Specifically, 142 different configurations have been randomly chosen (they will be the same ones for the three scenarios). Among them, 131 correspond to cases where the combined

³Two animations have been included as supplementary material for the reader showing numerous configurations examples and their amplitude PDF for the three studied scenarios.

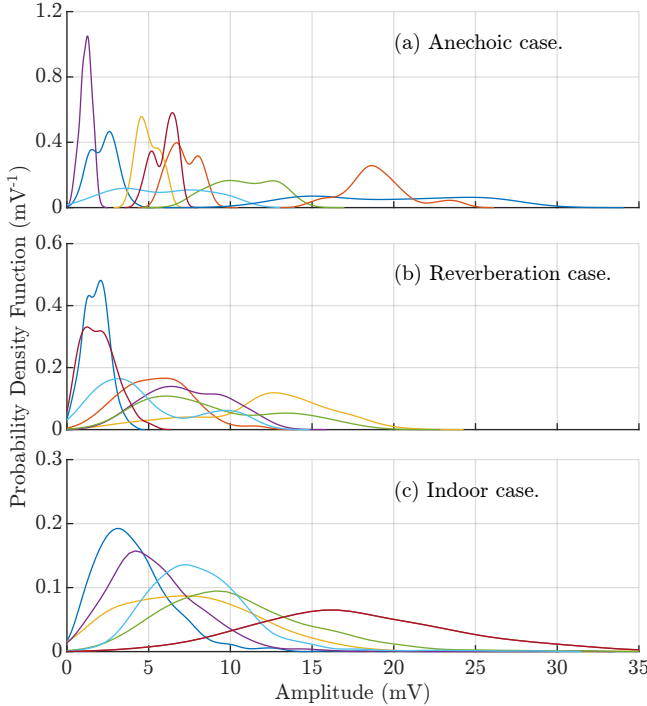


Fig. 3. PDFs associated with some examples of merged channels for the three scenarios. Each color represents one individual channel configuration. A great diversity of behaviors is observed (e.g. Rician- and Rayleigh-like, multimodality...).

pairs share a common Tx orientation, and 11 to pairs sharing a common Rx array position. To avoid possible biases, each sub-set has been previously analyzed. In the first case, it has been checked that the distribution of distances between the positions of the selected pairs is approximately equal to the distribution of all the possible pairs in the Rx array. On the other hand, combinations of different Tx orientations lead to three situations: same polarization but different pointing, same pointing but different polarization, and different pointing and polarization. It has been checked that the random sub-set includes combinations of the three types.

For a fair comparison, the 142 selected configurations are the same for anechoic, reverberation, and indoor scenarios. For the last one, as previously mentioned, the azimuth angle swept -30° , -15° , and 0° instead of -30° , 0° , and 30° . This implies that configurations of anechoic and reverberation scenarios cannot be replicated exactly for the indoor one. However, by tagging the angles as -1, 0, and 1 respectively in both cases, combinations can be computed while keeping the same tag for the three scenarios.

As a result of performing the linear combinations, a great diversity of channels emerges. Fig. 3 shows some amplitude PDF examples for the three scenarios. A multitude of behaviors are observed: Rician- and Rayleigh-like, multimodality... These latter are especially common in the anechoic configurations⁴.

⁴While the merged channels in anechoic case should correspond to a two-ray case by construction, in situations with very reduced multipath the CLT does not apply; hence, additional rays (e.g., those arising from reflections in the posts in Fig. 1) need to be accounted for individually. In this circumstance, the effect of these rays is translated into some additional modality [30].

Bimodality is a particular behavior where two local maxima appear. Ideally, they result from the presence of two rays whose power is substantially higher than the diffuse one or the noise floor [8]. In the case of our experimental measurements, the merged channels are computed to guarantee the presence of (at least) two specular components arriving the receiver.

IV. EMPIRICAL VALIDATION AND ANALYSIS

A. IFTR channel fitting

Once the Tx-Rx configurations have been selected, a fitting between the empirical PDFs and the IFTR theoretical one is carried out. A common way is the use of optimization numerical methods such as gradient descent algorithms (GDAs) or genetic algorithms (GA) to minimize an objective function. In this work, a multi-objective optimization problem has been defined with the following set of error metrics⁵ as targets:

- Mean Squared Error:

$$\text{MSE} \triangleq \frac{1}{N} \sum_{i=1}^N (f_{\text{exp}}(x_i) - f_{\text{mod}}(x_i))^2. \quad (9)$$

- Root Mean Squared Error:

$$\text{RMSE} \triangleq \sqrt{\frac{1}{N} \sum_{i=1}^N (f_{\text{exp}}(x_i) - f_{\text{mod}}(x_i))^2}. \quad (10)$$

- Mean Absolute Error:

$$\text{MAE} \triangleq \frac{1}{N} \sum_{i=1}^N |f_{\text{exp}}(x_i) - f_{\text{mod}}(x_i)|. \quad (11)$$

- Modified Kolmogorov-Smirnov statistic:

$$\text{KS} \triangleq \max_{x_i} |f_{\text{exp}}(x_i) - f_{\text{mod}}(x_i)|. \quad (12)$$

The use of multiple objective functions aims to find differences between the results when minimizing each error metric.

To solve the optimization problem, the chosen algorithm is the NSGA-II [31], an elitist GA designed for working with real numbers. It has been configured with a population size of 200 and a number of generations equal to 400. The elite count parameter (number of individuals guaranteed to survive to the next generation) has been established to the 5% of the population size. The algorithm has been configured to stop when 100 generations occur consecutively without significant changes in the solutions, which means they have converged. In addition, we have defined upper and lower bounds for limiting the search inside the solutions space. For the K factor, we have restricted the search to the interval from 0 to 10^3 . On the other hand, for the m_1 and m_2 parameters we have set 0 and 50 as upper and lower limits respectively. Finally, since the Δ parameter takes values in the interval $[0,1]$, the search has been bounded to the complete definition domain.

For each fitted channel, the output of the GA is a set of N_p solutions known as Pareto front. Solutions consist of a tuple of the form (K, Δ, m_1, m_2) representing one compromise

⁵The $f_{\text{exp}}(x)$ and $f_{\text{mod}}(x)$ functions represent the empirical and the IFTR channel model PDFs respectively. N corresponds with the number of points for representing the PDFs and is equal to 100 in all the studied configurations.

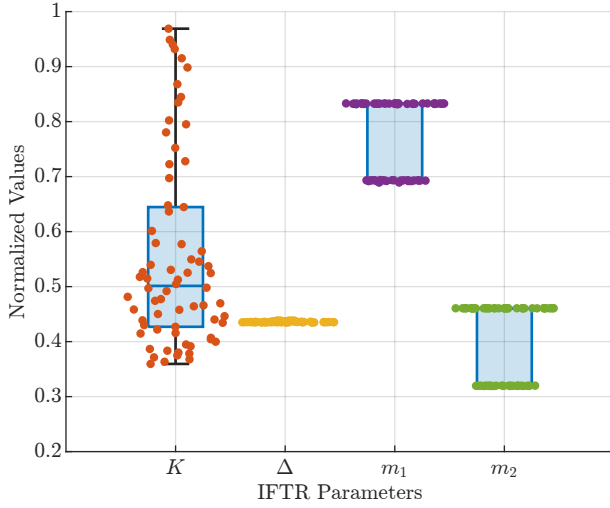


Fig. 4. Boxplot diagrams of the IFTR parameters for the Pareto front obtained for the anechoic configuration A. The individual points represent the solutions for each parameter, whereas the boxplots show their distribution. Values are normalized with respect to the upper limits established for the GA optimization search (that is, K w.r.t. 10^3 ; and m_1 and m_2 w.r.t. 30).

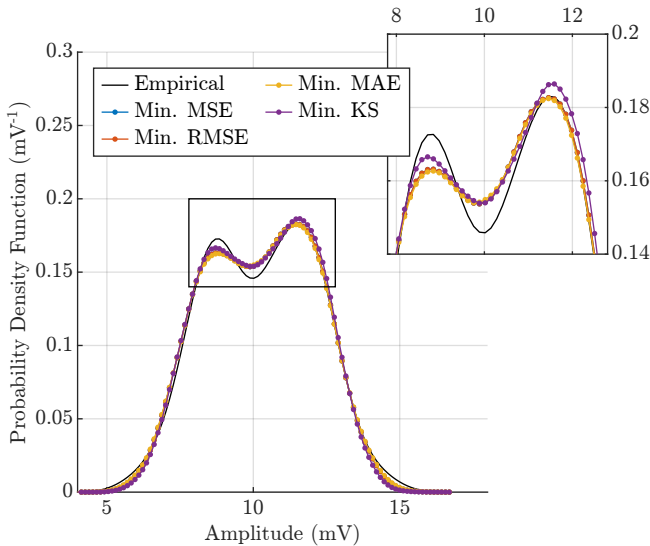


Fig. 5. IFTR PDF fitting results obtained for the anechoic configuration A minimizing each error metric. The empirical PDF is included as a reference.

situation between the four objective functions. For instance, Fig. 4 shows the solutions obtained for the Pareto front of configuration A (see Fig. 2) in the anechoic case. Boxplot diagrams and swarm-chart scatter plots are represented jointly for each parameter (normalized with respect to its upper bound). The K factor is distributed along a large interval which ranges from 0.36 to 0.97 (or equivalently from 25.6 dB to 29.8 dB, units no-normalized). However, most of the solutions are distributed near the median value of 0.50 (27.0 dB). In contrast, the Δ parameter practically does not change taking the same value of 0.44 for all the solutions tuples. Differences appear for the fluctuation parameters m_1 and m_2 , emerging two well-defined values. Specifically, for the parameter m_1 are obtained 0.69 and 0.83 (34.5 and 41.5 in no-normalized units); meanwhile for the m_2 are obtained 0.32 and 0.46 (16 and 23

without normalizing). This particular behavior is common for the majority of the studied merged channel configurations in the three scenarios.

We can focus our attention on the solutions tied to the minimum of each error metric (see Table I). The two extreme values for the pair m_1 and m_2 are either associated to the average error metrics (MSE, RMS and MAE), or to the distance error metric (KS), respectively. As previously mentioned, Δ remains almost unchanged in the four solutions tuples. On the other hand, the K factor is equal for the MSE and the RMSE solutions and differs roughly 1 dB with those obtained for the MAE and KS solutions. Fig. 5 shows the experimental PDF of the anechoic configuration A and the theoretical IFTR curves for each of the mentioned solutions, which are practically overlapped between each other. On the one hand, the PDFs associated with the MSE, RMSE and MAE error metrics have the same shape (quasi-equal IFTR parameters). On the other hand, the curve of the minimum KS is slightly different improving the fitting on the modal regions at the expense of the distribution tails. The latter are fitted with more accuracy by minimizing the mean errors.

To choose a particular solution $\hat{S} = (K, \Delta, m_1, m_2)$ from the Pareto front, we need some unified criterion. For that purpose, we first define the normalized error functions. As an example, the normalized MSE_n function is computed as

$$MSE_n(S) = \frac{MSE(S)}{\max_P MSE(P)}. \quad (13)$$

The normalization factor represents the maximum error metric obtained from among all the solutions of the Pareto front. Definition of $RMSE_n$, MAE_n and KS_n functions is completely analogous. From them, we can define a normalized metric ε_n as follows:

$$\varepsilon_n(S) \triangleq \frac{MSE_n + RMSE_n + MAE_n + KS_n}{4} \Big|_S. \quad (14)$$

Thus, selected solution \hat{S} will correspond with the S that minimize the metric ε_n , that is

$$\hat{S} = \min_S \varepsilon_n(S). \quad (15)$$

The cumulative density functions (CDFs) of the optimal IFTR parameters for each scenario have been represented in Fig. 6. A high contrast between anechoic and multipath⁶ scenarios is observed, with clear different trends.

Fig. 6(a) shows that the Rician-like K factor takes higher values on the anechoic configurations, which is due to the absence of diffuse power. In fact, the median value for this scenario is 28.3 dB, whereas for the multipath ones is 24.7 dB; that is, 3.6 dB of difference. On the other hand, as can be observed in Fig. 6(b), the Δ parameter in the anechoic case distributes along lower values than for the multipath configurations. That is a consequence of the lack of reflections in the anechoic scenario, where only the two specular rays are relevant and their amplitudes are significantly different. Moreover, it is also remarkable that anechoic and reverberation

⁶The term ‘‘multipath’’ refers, henceforth, to both reverberation and indoor propagation scenarios.

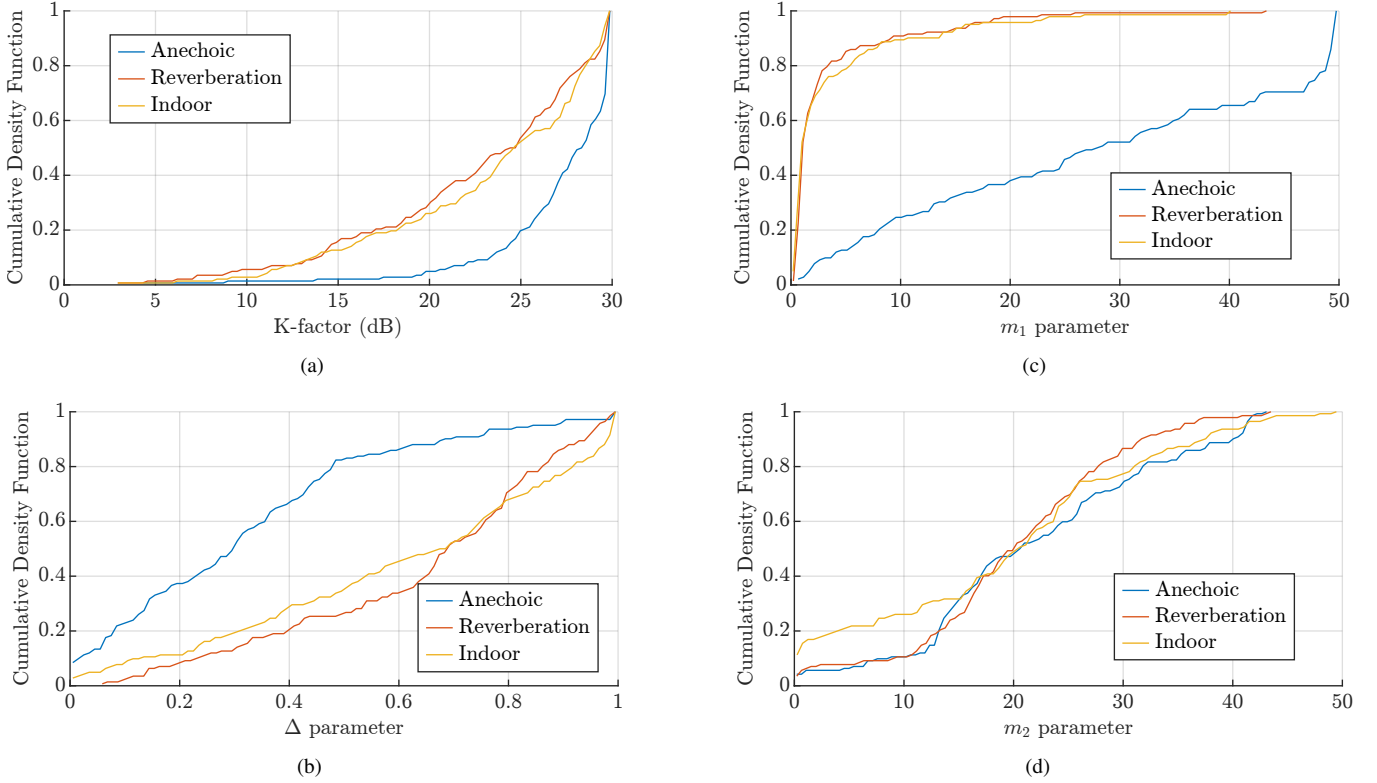


Fig. 6. Comparison of the optimal IFTR parameters CDFs for the three analysed environments.

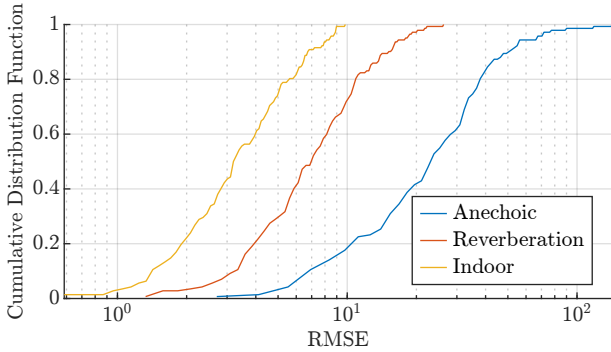


Fig. 7. RMSE metric CDFs for the optimal IFTR solutions.

TABLE I
IFTR PARAMETERS FOR EACH MINIMUM ERROR METRIC SOLUTION OF
THE PARETO FRONT IN ANECHOIC CONFIGURATION A

Parameter	Min. Error Metric Solutions (Conf. A)			
	MSE	RMSE	MAE	KS
Min. error	16.56	4.07	2.96	8.18
K [dB]	28.6	28.6	27.2	27.3
Δ	0.44	0.44	0.44	0.44
(m_1, m_2)	(35, 16)	(35, 16)	(35, 16)	(42, 23)

scenarios are the inverse of each other. For the latter, the multipath specular components that arrive at the antenna have similar amplitudes. That, in addition to the nLoS situation,

imposes Δ taking higher values. The obtained median values are 0.30 for the anechoic case and 0.69 for reverberation and indoor scenarios. Although these two latter take the same median value, slight differences are observed between their distributions. For Δ values lower than the median, the distribution for the indoor configurations is higher than for the reverberation ones. In contrast, for higher Δ values, the roles are exchanged and the distribution becomes lower for the indoor case. This is explained by the mixed character of these types of scenarios. The studied indoor measurements combine the LoS situation with a rich multipath. The high power of the LoS rays produces an imbalance between the amplitudes of the received rays which implies a reduction of the Δ parameter.

The m_1 and m_2 fluctuation parameters distributions are depicted in Figs. 6(c) and 6(d). The first ray is more fluctuating in the reverberation and indoor scenarios than in the anechoic ones since the m_1 parameter is distributed along low values (the medians are 1 and 28 respectively). That is due to the multipath effect, which provides more accentuated variations in the received signal. This also explains that distribution for reverberation and indoor are overlapped between each other. On the other hand, the m_2 parameter takes higher values than the m_1 in the multipath scenarios (median values of 20 and 21 respectively). This implies that, generally, the second ray is less fluctuating than the first for the reverberation and indoor cases, whereas for the anechoic both rays have reduced fluctuation. Nevertheless, for the indoor configurations, there exists a remarkable percentage of channels with a low m_2 parameter which is related to a significant multipath effect.

TABLE II
NUMERICAL RESULTS OF THE GIVEN FITTING EXAMPLE CONFIGURATIONS IN THE THREE STUDIED SCENARIOS

Parameter	Scenario	Configuration					
		A	B	C	D	E	F
K [dB]	Anechoic	29.3	27.8	29.9	25.0	29.9	30.0
	Reverberation	25.8	27.3	29.4	29.8	22.7	26.3
	Indoor	22.8	25.6	29.9	27.1	29.9	20.6
Δ	Anechoic	0.44	0.09	0.23	1.00	0.45	0.21
	Reverberation	0.09	0.80	0.49	0.73	0.33	0.52
	Indoor	0.58	0.24	0.02	1.00	0.54	0.99
(m_1, m_2)	Anechoic	(35, 16)	(27, 13)	(50, 35)	(11, 22)	(36, 12)	(50, 14)
	Reverberation	(12, 19)	(1, 18)	(1, 33)	(0.60, 0.39)	(15, 27)	(3, 32)
	Indoor	(0.69, 19)	(0.93, 22)	(0.46, 15)	(5, 38)	(1, 25)	(2, 25)
RMSE	Anechoic	4.10	16.46	26.51	33.48	9.10	16.64
	Reverberation	4.00	9.71	4.22	10.41	3.10	2.46
	Indoor	4.30	3.52	8.86	4.24	1.10	3.29

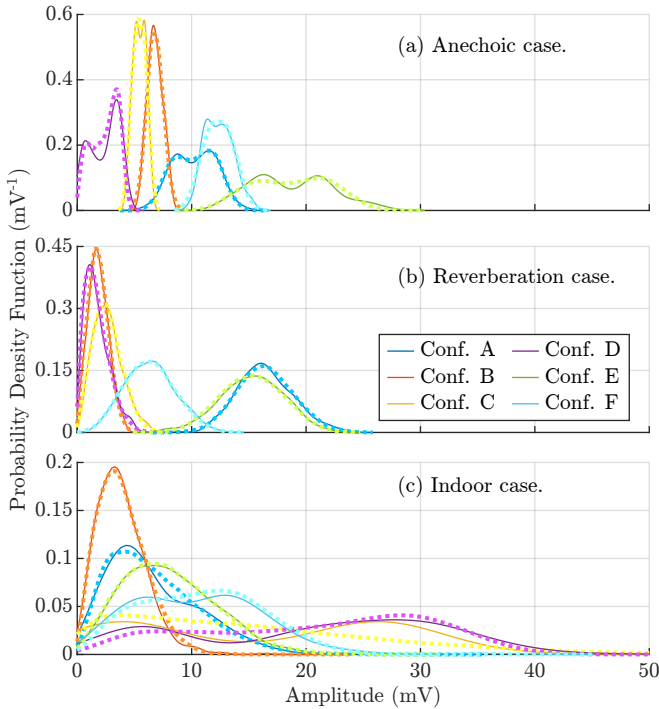


Fig. 8. PDF fitting examples for different configurations. Solid and dotted lines represent empirical and IFTR model distributions respectively.

To compare the fitting accuracy between the analyzed scenarios, the RMSE metric associated with each solution has been studied. Fig. 7 shows the CDFs for the three scenarios. The lowest error is obtained for the indoor case, with a median value of 3.2; whereas for the reverberation and anechoic cases the medians are 7.0 and 23.0 respectively. From this, it can be affirmed that the IFTR model describes properly rich multipath scenarios in both LoS and nLoS situations. The largest RMSE

values correspond to the anechoic case. As it will be discussed later, this is due to a non-uniform phase distribution in the received signal providing some contradictions with the IFTR model underlying assumptions.

Some particular fitting examples⁷ configurations (namely as A, B, C, D, E, and F) are depicted in Fig. 8. A good fitting accuracy is observed for the three scenarios, and the particular numerical results can be consulted in Table II. Bimodal behaviors are accurately modeled, as well as Rician- and Rayleigh-like ones common in multipath scenarios. Specifically, the IFTR model is capable of reproducing bimodality as long as K takes large values and Δ is near to one. These conditions are equivalent to those explained in Section III for experimental bimodality. That is, the power of the first ray has to be comparable to the one of the second ray, and both have to be notably higher than the diffuse one.

Fig. 9 shows the specific configurations of the given examples in terms of the two combined Rx array positions (points with the same color) jointly with the common Tx orientation. Positions are referred with respect to the array center, which corresponds to the (0,0) coordinate.

B. Anechoic environment analysis

As previously mentioned, anechoic scenarios are associated with higher fitting error than multipath ones (see Fig. 7). Although most of the configurations can be described with high accuracy, there exists a certain percentage of fitted configurations with an unsatisfactory goodness of fit (GoF). After a thorough analysis, the key aspect that justifies this behavior is the lack of phase diversity in certain combinations. That is, the traveled path by the waves and the deep attenuation of diffuse

⁷As supplementary material for the reader, an additional animation is included showing the obtained fitting solutions for each of the 142 configurations in the three studied scenarios.

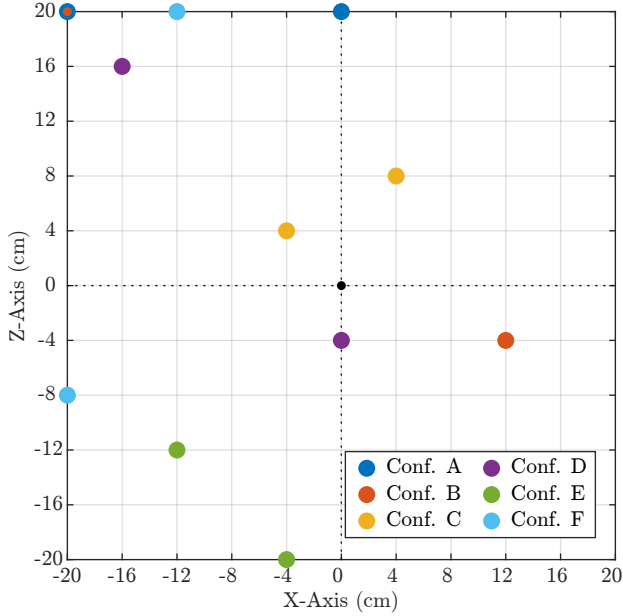


Fig. 9. Configurations of the given fitted channel examples. Each pair of points with the same color identifies the two Rx array positions that compose the merged channel. The common Tx orientations (as tags) for each configuration are: $\{\phi, \beta\} = \{0, 0\}$ for A, E, and F; $\{\phi, \beta\} = \{-1, 0\}$ for B; and $\{\phi, \beta\} = \{1, 1\}$ for C and D.

components is insufficient to produce all phase differences between $-\pi$ and π . This has two main implications: on the one hand, it causes the CLT assumption for the diffuse component is not met; on the other hand, it affects the assumption of uniformly distributed phases for the dominant specular components. The latter is of importance because you can write the received amplitude of the IFTR model in terms of the phase difference α as follows:

$$V_r = \exp(j\varphi_1) (A_1 + A_2 \exp(j\alpha)) + Z, \quad (16)$$

where $\alpha = \varphi_2 - \varphi_1$ follows an uniform distribution in the range from $-\pi$ to π .

The implications of a non-uniform phase distribution have been discussed in [21], where the TWDP model was modified to account for this particular situation. The resulting model, termed as generalized two-ray model with von Mises phase distribution (GTR-V), has the following PDF for the received amplitude r :

$$f_{\text{GTR-V}}(r) = \int_{-\pi}^{\pi} f_{\text{rice}}(r; K[1 + \Delta \cos(\alpha)]) f_{\alpha}(\alpha) d\alpha, \quad (17)$$

where $f_{\text{rice}}(r, K_r)$ is the well-known Rician distribution with a factor $K_r = K[1 + \Delta \cos(\alpha)]$. The PDF is given by

$$f_{\text{rice}}(r; K_r) = \frac{r}{\sigma^2} \exp\left(-\frac{r^2}{2\sigma^2} - K_r\right) I_0\left(\frac{r}{\sigma} \sqrt{2K_r}\right), \quad (18)$$

with $I_0(x)$ being the modified Bessel function of first class and order zero. On the other hand, $f_{\alpha}(\alpha)$ represents the phase difference distribution. In the GTR-V channel model, it corresponds to a von Mises PDF [32]:

$$f_{\alpha}(\alpha; \kappa, \phi) = \frac{\exp(\kappa \cos(\alpha - \phi))}{2\pi I_0(\kappa)} \quad \forall \alpha \in [-\pi, \pi], \quad (19)$$

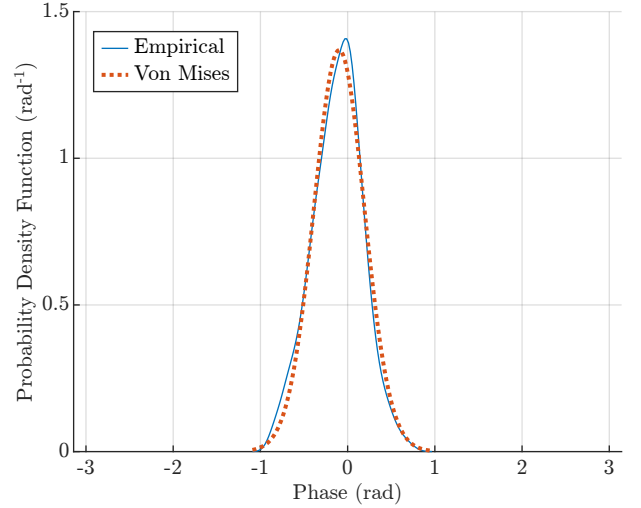


Fig. 10. Phase difference fitting with von Mises distribution for the anechoic configuration G.

where $\phi \in \mathbb{R}$ represents the mean of the distribution and $\kappa \geq 0$ is inversely related to its variance.

Indeed, it is possible to generalize the IFTR model to incorporate the effect of a non-uniform phase distribution following the rationale in [21]. Nevertheless, this would imply that the resulting model would have two additional parameters, incurring additional complexity when it comes to fitting. Instead, we will use the GTR-V model even though it has no fluctuation on the two dominant specular components; in practice, this is equivalent to assuming a sufficiently large value of m_1 and m_2 in the IFTR model (see Fig. 6). Therefore, the use of this alternative model is well-justified for the sake of simplicity. After analyzing the distribution of the phase difference between the dominant specular components in the relevant anechoic configurations, a small sub-set with von Mises-like PDF for phase difference has been selected (named configurations G, H, and I).

The fitting process for the GTR-V model has been carried out as a two-step optimization problem. First, the empirical phase difference distribution is modeled as a von Mises distribution, finding the two parameters ϕ and κ that provide the best fit for the phase difference distribution. After finding these parameters, a second optimization is performed analogously as for the IFTR model, finding the best pair $\{K, \Delta\}$ for the GTR-V model applying a GA search.

Fig. 10 shows the fitting of the phase difference distribution⁸ with a von Mises PDF for configuration G. After the first step of the optimization, the resulting parameters κ and ϕ yield an MSE of 0.0029, which implies an excellent GoF. This process has been carried out also for H and I configurations. The next step is to find the optimal K and Δ parameters for the GTR-V model by the use of GA. The obtained results for the configurations G, H, and I are summarized in Table III, comparing them with the obtained for the IFTR model. In

⁸Though the channel measurements include both diffuse and specular components, in anechoic channels the LoS ray power is significantly the highest. Thus, it is reasonable to estimate the phase difference distribution as the PDF of the phase difference of the two merged channels.

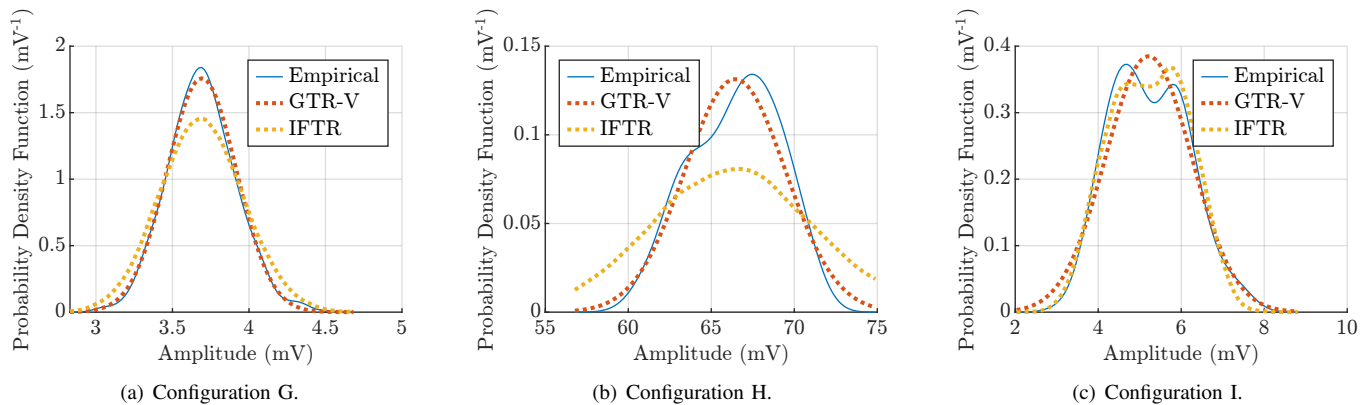
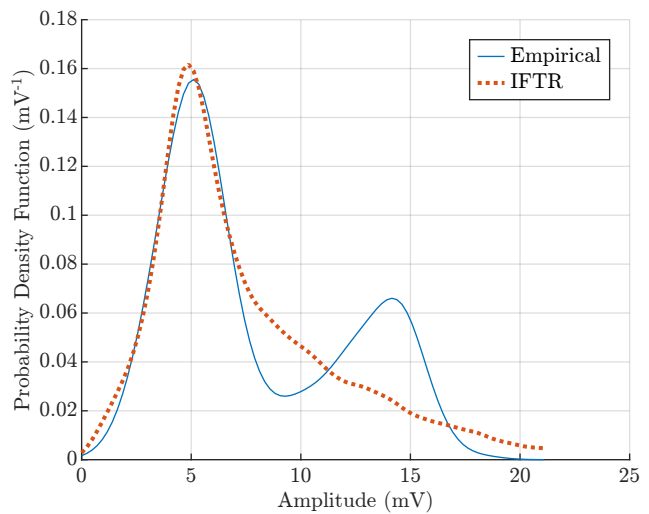


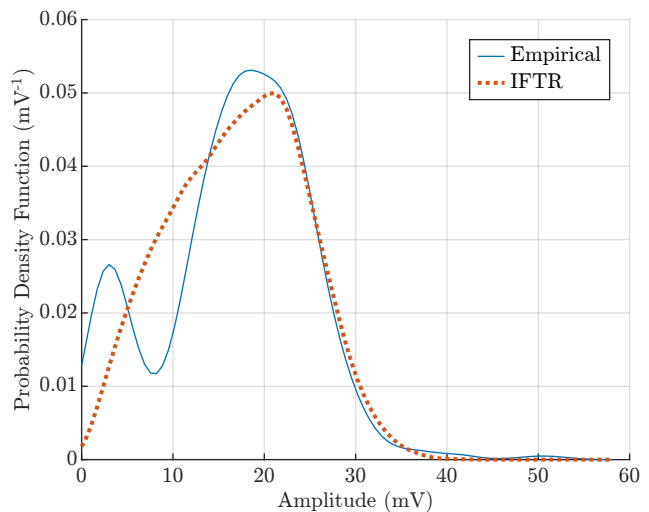
Fig. 11. Comparison between fitted IFTR and GTR-V PDFs for some particular anechoic configurations.

TABLE III
NUMERICAL RESULTS COMPARISON BETWEEN THE IFTR AND THE
GTR-V MODELS

Model	Parameter	Anechoic configuration		
		G	H	I
IFTR	K [dB]	30.0	30.0	25.1
	Δ	2.7×10^{-3}	0.7×10^{-3}	0.40
	(m_1, m_2)	(50, 32)	(50, 5)	(31, 13)
	RMSE	142.38	28.17	17.58
GTR-V	K [dB]	19.8	23.8	10.6
	Δ	0.45	2.6×10^{-4}	0.11
	ϕ	-0.10	0.08	-0.10
	κ	12.04	638.94	1.23
	MSE_{VM}	2.9×10^{-3}	0.19	6.2×10^{-4}
	RMSE	37.66	10.04	28.66



(a) Configuration J (reverberation).



(b) Configuration K (indoor).

addition, the obtained PDFs are depicted in Fig. 11. For configurations G and H [Figs. 11(a) and 11(b)], we see that the GTR-V model provides better results than the IFTR one. The effect of a non-uniform phase distribution is translated into an effective reduction of the variance, and it can be visually confirmed that the GTR-V model achieves this. However, we see that the fitting is not improved when the empirical PDF is bimodal – see configuration I in Fig. 11(c). The capabilities of the TWDP model to capture bimodality are affected when a non-uniform phase difference distribution is considered in the GTR-V model.

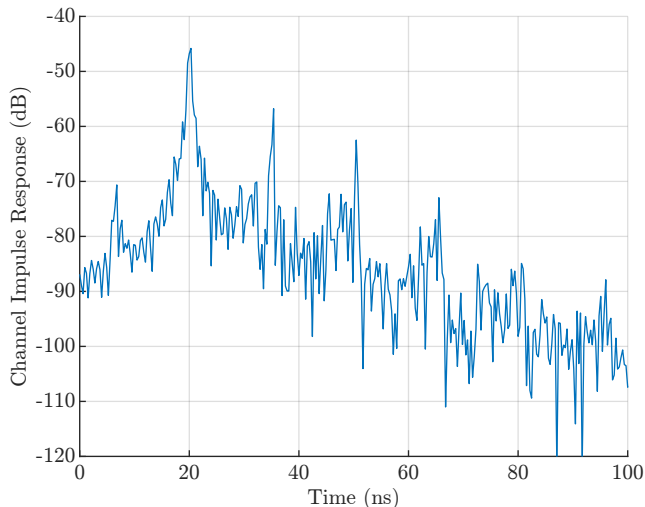
C. Multipath environments analysis

Multipath environments have lower RMSEs compared to the anechoic ones, as has been shown in Fig. 7. This implies that most of the configurations have been described correctly with the IFTR model. However, we have identified some cases in which the fitting fails. Specifically, in the cases of sharp bimodal behaviors, the ability of the IFTR model to capture such bimodality is not enough. This is exemplified in

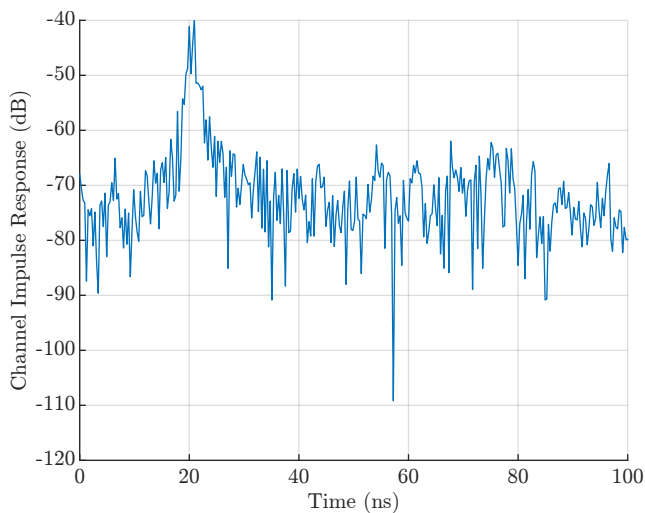
Fig. 12. PDFs empirical and fitted for sharp bimodality behaviors.

TABLE IV
IFTR NUMERICAL RESULTS OBTAINED FOR MULTIPATH CONFIGURATIONS
WITH SHARP BIMODALITY BEHAVIORS

Parameter	Multipath configuration	
	J (reverberation)	K (indoor)
K [dB]	28.9	28.2
Δ	0.92	0.87
(m_1, m_2)	(0.45, 30)	(3, 31)
RMSE	18.27	6.33



(a) Configuration J (reverberation).



(b) Configuration K (indoor).

Fig. 13. CIR for multipath configurations with sharp bimodality behaviors.

Fig. 12 for another configurations J and K in reverberation and indoor environments respectively. In these situations, the model tries to fit the dominant peak but masks the secondary one. Numerical results can be consulted in Table IV.

One way to determine the origin of these particular behaviors is to analyze the CIR of the configuration. Fig. 13 shows

the estimation of the channel time responses. On the one hand, Fig. 13(a) depicts the CIR for the reverberation configuration J. It is clear that more than two rays are arriving at the antenna with power significantly high and comparable between each other. This is not covered by the IFTR model. Even though the consideration of additional rays can be usually encompassed by integrating these into the diffuse component [30], this is not the case when the overall number of rays is reduced, multipath propagation is limited, and there is a lack of phase richness in the propagation environment. On the other hand, Fig. 13(b) presents the CIR for the indoor configuration J. Two dominant rays are observed, but they are overlapped in time between each other. Hence, its interaction may not be described independently as the IFTR model assumes. The sharp bimodality behavior appears as a cause of the time interaction of these two rays.

V. CONCLUSIONS

We conducted an empirical validation of the independent fluctuating two-ray (IFTR) fading model, covering a wide range of scenarios in the frequency band n258 (from 24.25 GHz to 27.5 GHz). We confirmed that the IFTR model is highly versatile, and is able to recreate rather dissimilar propagation conditions including anechoic, reverberation, and indoor scenarios. Besides, the four shape parameters that characterize the model have a solid physical meaning, which agrees with the expected properties of each analyzed channel.

We also observed some relevant effects that put forth the limitations of the IFTR model: (i) the assumption of uniform phases for the dominant specular components does not always hold, especially when there is a lack of phase richness. This is the case in scenarios with a reduced multipath, and is likely to become a dominant effect as we move up in frequency; (ii) the IFTR model is not able to capture sharp bimodal behaviors observed in some of the measurements. This can be caused by the combination of a number of effects, such as the presence of additional rays (due to spurious reflections), the absence of rich multipath propagation, and the interaction between dominant specular components. In this regard, the development of physically-motivated models that capture these behaviors deserves special attention, together with additional empirical validations at higher frequencies.

APPENDIX

The supplementary material is available at the IEEE DataPort repository: <https://dx.doi.org/10.21227/hzw9-6q21>. It consists of three different animations, where two of them present the channel diversity along the computed combinations and the other one the obtained solutions for the IFTR fitting. The former shows multitude of configurations with a representative scheme, the associated PDF of received amplitude for each scenario, and the phase difference PDF. The latter represents the obtained solutions for the Pareto front, the distribution of the IFTR parameters and the RMSE metric, the phase PDF, and the associated configuration scheme.

REFERENCES

- [1] T. S. Rappaport, Y. Xing, G. R. MacCartney, A. F. Molisch, E. Mellios and J. Zhang, "Overview of Millimeter Wave Communications for Fifth-Generation (5G) Wireless Networks—With a Focus on Propagation Models," *IEEE Transactions on Antennas and Propagation*, vol. 65, no. 12, pp. 6213-6230, 2017.
- [2] M. Polese, J. M. Jornet, T. Melodia and M. Zorzi, "Toward End-to-End, Full-Stack 6G Terahertz Networks," *IEEE Communications Magazine*, vol. 58, no. 11, pp. 48-54, 2020.
- [3] D. W. Matolak, "Channel Modeling for Vehicle-To-Vehicle Communications," *IEEE Communications Magazine*, vol. 46, no. 5, pp. 76-83, 2008.
- [4] COST Action 231 (Project) and European Commission. "DGXIII Telecommunications, Information Market, and Exploitation of Research," *Digital Mobile Radio Towards Future Generation Systems: Final Report*. European Commission, Directorate-General Telecommunications, Information Society, Information Market and Exploitation of Research, 1999.
- [5] Technical Specification Group Radio Access Network, "Study on channel model for frequencies from 0.5 to 100 GHz (Release 17)," 3rd Generation Partnership Project, 3GPP TR 38.901 v17.0.0, 2022.
- [6] M. Lecci, P. Testolina, M. Polese, M. Giordani and M. Zorzi, "Accuracy Versus Complexity for mmWave Ray-Tracing: A Full Stack Perspective," *IEEE Transactions on Wireless Communications*, vol. 20, no. 12, pp. 7826-7841, 2021.
- [7] M. K. Simon and M.-S. Alouini, "Digital Communication over Fading Channels", 2nd ed. Hoboken, NJ, USA: Wiley, 2005.
- [8] G. D. Durgin, T. S. Rappaport and D. A. de Wolf, "New analytical models and probability density functions for fading in wireless communications," *IEEE Transactions on Communications*, vol. 50, no. 6, pp. 1005-1015, 2002.
- [9] J. Frolik, "On appropriate models for characterizing hyper-rayleigh fading," *IEEE Transactions on Wireless Communications*, vol. 7, no. 12, pp. 5202-5207, 2008.
- [10] J. M. Romero-Jerez, F. J. Lopez-Martinez, J. F. Paris and A. J. Goldsmith, "The Fluctuating Two-Ray Fading Model: Statistical Characterization and Performance Analysis," *IEEE Transactions on Wireless Communications*, vol. 16, no. 7, pp. 4420-4432, 2017.
- [11] M. Olyaei, J. A. Cortés, F. J. Lopez-Martinez, J. F. Paris and J. M. Romero-Jerez, "The Fluctuating Two-Ray Fading Model With Independent Specular Components," *IEEE Transactions on Vehicular Technology*, vol. 72, no. 5, pp. 5533-5545, 2023.
- [12] A. Abdi, W. C. Lau, M. . -S. Alouini and M. Kaveh, "A new simple model for land mobile satellite channels: first- and second-order statistics," *IEEE Transactions on Wireless Communications*, vol. 2, no. 3, pp. 519-528, 2003.
- [13] J. F. Paris, "Statistical Characterization of κ - μ Shadowed Fading," *IEEE Transactions on Vehicular Technology*, vol. 63, no. 2, pp. 518-526, 2014.
- [14] M. Pagin, S. Lagén, B. Bojovic, M. Polese and M. Zorzi, "Improving the Efficiency of MIMO Simulations in ns-3," in *2023 Workshop on ns-3 (WNS3 2023)*, Arlington, VA, USA. ACM, New York, NY, USA, pp. 1-9, 2023.
- [15] E. Zöchmann et al., "Position-Specific Statistics of 60 GHz Vehicular Channels During Overtaking," *IEEE Access*, vol. 7, pp. 14216-14232, 2019.
- [16] K. Yang et al., "Propagation measurements of mobile radio channel over sea at 5.9 GHz," in *2018 16th International Conference on Intelligent Transportation Systems Telecommunications (ITST)*, Lisboa, Portugal, pp. 1-5, 2018.
- [17] C. L. Holloway, D. A. Hill, J. M. Ladbury, P. F. Wilson, G. Koepke and J. Coder, "On the Use of Reverberation Chambers to Simulate a Rician Radio Environment for the Testing of Wireless Devices," *IEEE Transactions on Antennas and Propagation*, vol. 54, no. 11, pp. 3167-3177, 2006.
- [18] J. Frolik, T. M. Weller, S. DiStasi and J. Cooper, "A Compact Reverberation Chamber for Hyper-Rayleigh Channel Emulation," *IEEE Transactions on Antennas and Propagation*, vol. 57, no. 12, pp. 3962-3968, 2009.
- [19] J. D. Sanchez-Heredia, J. F. Valenzuela-Valdes, A. M. Martinez-Gonzalez and D. A. Sanchez-Hernandez, "Emulation of MIMO Rician-Fading Environments With Mode-Stirred Reverberation Chambers," *IEEE Transactions on Antennas and Propagation*, vol. 59, no. 2, pp. 654-660, 2011.
- [20] 3rd Generation Partnership Project, "5G; NR; User Equipment (UE) radio transmission and reception; Part 2: Range 2 Standalone (Release 17)," European Telecommunications Standards Institute, 3GPP TS 38.101-2 v17.5.0, 2022.
- [21] M. Rao, F. J. Lopez-Martinez, M. -S. Alouini and A. Goldsmith, "MGF Approach to the Analysis of Generalized Two-Ray Fading Models," *IEEE Transactions on Wireless Communications*, vol. 14, no. 5, pp. 2548-2561, 2015.
- [22] G. D. Durgin, "Theory of stochastic local area channel modeling for wireless communications," Ph.D. thesis, Virginia Polytechnic Institute and State University, Blacksburg, Virginia, 2000.
- [23] H. M. Srivastava and P. W. Karlsson, "Introduction and Definitions," in *Multiple Gaussian Hypergeometric* Wiley, 1st ed. Chichester, England: Wiley, 1985, ch. 1, sec. 1.4, pp. 33-41.
- [24] M. Olyaei, H. Hashemi and J. M. Romero-Jerez, "A Tractable Statistical Representation of IFTR Fading with Applications," to appear in *IEEE Transactions on Communications*, 2024.
- [25] B. Selim, O. Alhoussein, S. Muhaidat, G. K. Karagiannidis and J. Liang, "Modeling and Analysis of Wireless Channels via the Mixture of Gaussian Distribution," *IEEE Transactions on Vehicular Technology*, vol. 65, no. 10, pp. 8309-8321, 2016.
- [26] E. N. Pappasotiriou, A. A. Boulogeorgos, and A. Alexiou, "Outdoor THz fading modeling by means of gaussian and gamma mixture distributions," *Scientific Reports*, vol. 13, no. 1, 2023.
- [27] A. Ramírez-Arroyo, L. García, A. Alex-Amor and J. F. Valenzuela-Valdés, "Artificial Intelligence and Dimensionality Reduction: Tools for Approaching Future Communications," *IEEE Open Journal of the Communications Society*, vol. 3, pp. 475-492, 2022.
- [28] T. Wilding, B. J. B. Deutschmann, C. Nelson, X. Li, F. Tufvesson and K. Witrisal, "Propagation Modeling for Physically Large Arrays: Measurements and Multipath Component Visibility," in *2023 Joint European Conference on Networks and Communications & 6G Summit (EuCNC/6G Summit)*, Gothenburg, Sweden, pp. 204-209, 2023.
- [29] S. K. Thompson, "Sampling," John Wiley & Sons, Incorporated, 2012.
- [30] J. M. Romero-Jerez, F. J. Lopez-Martinez, J. P. Peña-Martín and A. Abdi, "Stochastic Fading Channel Models With Multiple Dominant Specular Components," *IEEE Transactions on Vehicular Technology*, vol. 71, no. 3, pp. 2229-2239, 2022.
- [31] K. Deb and D. Kalyanmoy, "Multi-Objective Optimization Using Evolutionary Algorithms," Chichester, England: Wiley, 2001.
- [32] R. V. Mises, "Über die 'Ganzzahligkeit' der Atomgewicht und verwandte Fragen," *Physikal. Z.*, vol. 19, pp. 490-500, 1918.